$Ca_3Mn_2O_7$ structural path unraveled by atomic-scale properties: A combined experimental and *ab initio* study

P. Rocha-Rodrigues,[1] S. S. M. Santos,[1] I. P. Miranda,[2] G. N. P. Oliveira,[1] J. G. Correia,[3] L. V. C. Assali,[2] H. M. Petrilli,[2] J. P. Araújo,[1] and A. M. L. Lopes[1,*]

[1]*IFIMUP, Institute of Physics for Advanced Materials, Nanotechnology and Photonics, Departamento de Física e Astronomia da Faculdade de Ciências da Universidade do Porto, Rua do Campo Alegre, 687, 4169-007 Porto, Portugal*

[2]*Instituto de Física, Universidade de São Paulo, 66318, 05315-970, São Paulo-SP, Brazil*

[3]*C2TN, Centro de Ciências e Tecnologias Nucleares, Departamento de Engenharia e Ciências Nucleares, Instituto Superior Técnico, Universidade de Lisboa, Estrada Nacional 10, 2695-066 Bobadela LRS, Portugal*

(Received 3 September 2019; revised manuscript received 13 December 2019; accepted 15 January 2020; published 12 February 2020)

The structural phase transition path from the low-temperature polar structure up to the highest symmetric phase in the hybrid improper ferroelectric $Ca_3Mn_2O_7$ compound is here investigated at atomic scale. Measurements using the perturbed angular correlation local probe technique are combined with *ab initio* electronic structure calculations to observe the evolution of the electric field gradient parameters at the Ca site within the 10–1200 K temperature range. The results show that polar-phase clusters persist at temperatures as high as 500 K. In addition, evidence is given for a structural phase transition occurring above 1150 K. The high-temperature symmetry is here confirmed to be $I4/mmm$.

DOI: 10.1103/PhysRevB.101.064103

I. INTRODUCTION

Naturally layered perovskites such as the Ruddlesden-Popper (RP) phases, with general formula $A_{n+1}B_nO_{3n+1}$ (A = rare-earth or alkaline-earth metal and B = transition metal) are studied as feasible routes to develop and design novel functional materials, ranging from superconductors, multiferroics, to materials that display negative thermal expansion [1–8]. The main subject of the present work, the $Ca_3Mn_2O_7$ compound, was studied by Benedek and Fennie [1] through first-principles density functional theory (DFT), proposing it as a prototypical multiferroic in which the ferroelectric and the ferromagnetic alignment arise from the same elastic lattice instability, providing an indirect but high magnetoelectric coupling mechanism. More recently, Senn *et al.* [7] showed experimentally that $Ca_3Mn_2O_7$ exhibits, for a certain temperature range, a uniaxial negative thermal expansion (UNTE), presenting a UNTE coefficient of ≈ -3.6 ppm/K [7]. The combined effect of octahedral distortions and the layered structure of the RP lattice proved to be essential for these two functional properties to emerge [1,3,8]. As depicted in Fig. 1(a), the $Ca_3Mn_2O_7$ structure consists of a series of stacked $CaMnO_3$ perovskite blocks intercalated periodically with rocksalt-like CaO layers. A hybrid improper ferroelectric (HIF) mechanism was predicted for the $Ca_3Mn_2O_7$ low-temperature ground state, which was known to exhibit an orthorhombic $A2_1am$ symmetry [1]. Here, the polar distortion zone center mode (Γ_5^-), involving the antiferroelectric displacement of Ca-site ions along the [100] direction which is represented in the inset of Fig. 1(a), acts as a secondary order parameter of the ferroelectric transition, being driven by the presence of two primary nonpolar MnO_6 octahedral rotation (X_2^+) and tilting (X_3^-) modes. The X_2^+ distortion involves the MnO_6 octahedral in-plane rotation around the [001] direction, whereas the X_3^- distortion is related to a tilting of the octahedra around the [100] axis; both octahedral distortion orientations are highlighted by the blue arrows in Fig. 1(a). The Ca cation antiferroelectric displacement mode was predicted to result in a net ferroelectric polarization of $\approx 5\ \mu C/cm^2$ and its orientation was shown to be reversed by changing the sign of the X_2^+ rotational or X_3^- tilting modes [1]. Below $Ca_3Mn_2O_7$ magnetic transition temperature (~115 K), the same X_3^- MnO_6 octahedral tilting produces a spin canting of the antiferromagnetic G-type ordering through the Dzyaloshinskii-Moriya interaction, and induces in this way, weakly ferromagnetic domains [1,9]. Benedek and Fennie further showed that the orientation of the net magnetization can be reversed by changing the X_3^- tilting mode, proposing that the common lattice distortion, at the origin of both ferroic orders, should provide an indirect mechanism to achieve a high magnetoelectric coupling [1].

Recently, evidences for hybrid improper ferroelectricity and magnetoelectric coupling in $Ca_3Mn_2O_7$ were observed experimentally by Liu *et al.* [11]. Ferroelectric hysteresis cycles were measured with the positive-up negative-down (PUND) method [12], exhibiting electric coercive fields of the order of 6 kV/cm at 10 K. Moreover, an abrupt reduction of the $Ca_3Mn_2O_7$ magnetization value was observed, under a 4 T magnetic field, when applying intense electric fields (E) above the measured ferroelectric coercive field of 6.25 kV/cm. A magnetization decrease as large as 3% was observed for $|E| = 10$ kV/cm. Unfortunately, the considerable high-conductivity character of the sample has prevented the observation of its

*armandina.lima.lopes@cern.ch

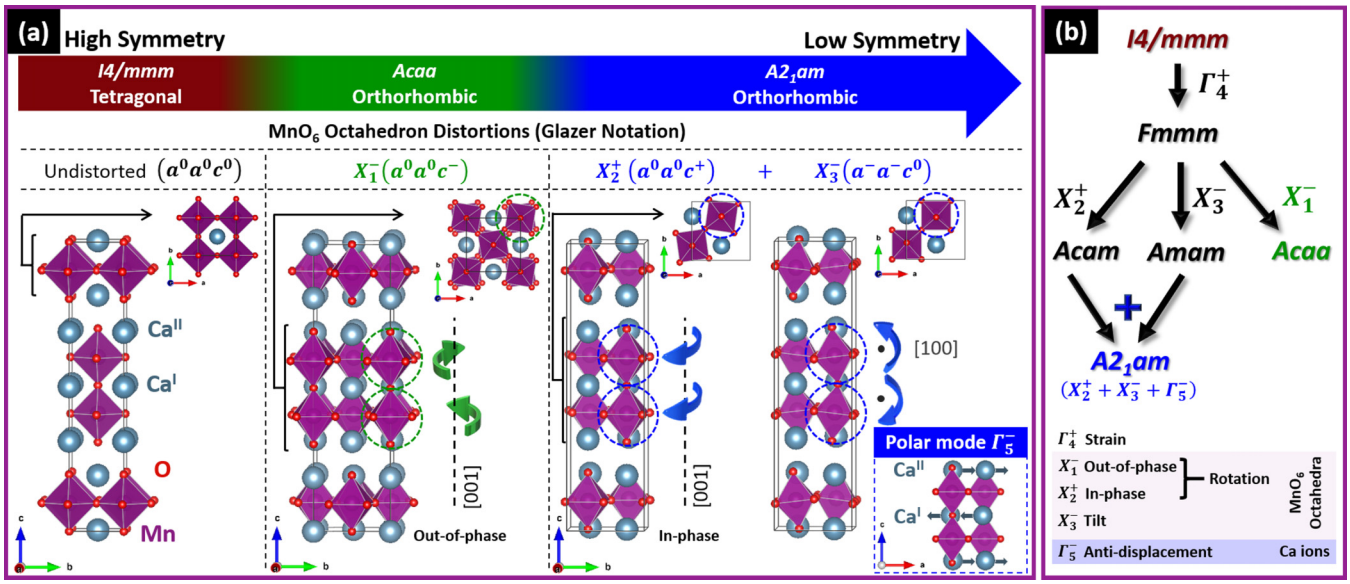

FIG. 1. (a) Schematic view of the $Ca_3Mn_2O_7$ structure in the undistorted aristotypical $I4/mmm$ symmetry and under the MnO_6 octahedral rotation and tilting modes for the experimentally observed $Acaa$ (X_1^-) and $A2_1am$ (X_2^-, X_3^-) structural phases [7]; the respective Glazer notations are also specified. Blue spheres represent Ca atoms, while Mn atoms are at the center of the octahedra, with an O atom at each apex. Green/blue arrows schematize the orientation of rotation and tilting of the MnO_6 octahedra that are enclosed by the green/blue dashed circles. The X_1^- out-of-phase and the X_2^+ in-phase rotation of MnO_6 octahedra present in the $Acaa$ and $A2_1am$ symmetries, and the orientation of the X_3^- tilting mode as well are highlighted. In the $A2_1am$ section, at the right bottom corner, the antiferroelectric displacement of Ca ions along the [100] direction, associated with the condensation of the polar mode of irrep Γ_5^-, established as a secondary order parameter of the HIF transition, driven by the condensation of the two nonpolar primary lattice instabilities, MnO_6 rotation (X_2^+) and tilting (X_3^-) modes [1] are depicted. (b) Space group symmetry relationship between the $I4/mmm$, the $Acaa$, and the $A2_1am$ structural phases, highlighting the fact that the $A2_1am$ space group does not form a subgroup of the $Acaa$ symmetry [7]. The presented $Fmmm$ structural phase regards the condensation of the orthorhombic lattice strain mode (Γ_4^+); however, the crystallographic data for the $Acaa$ structure [7] shows that this structure is pseudotetragonal such that the amplitude of the Γ_4^+ is null. The crystal structure representations were taken by VESTA software [10].

ferroelectric polarization for temperatures much higher than 25 K [11,13].

However, according to the experimental work based on high-resolution x-ray diffraction (XRD) and Rietveld analysis published by Senn *et al.* [7], it is known that the polar structure $A2_1am$ should nucleate upon cooling below 320 K in a first-order structural transition, from the higher temperature pseudotetragonal $Acaa$ symmetry [7]. By space group relations, the $Acaa$ phase is achieved from the aristotypical tetragonal $I4/mmm$ structural phase through condensation of a zone boundary X_1^- distortion mode, in which the MnO_6 octahedra display a rotation around the [001] direction, i.e., vertical neighbor MnO_6 octahedra (within a perovskite slab) undergo an out-of-phase rotation around the c axis, highlighted in Fig. 1(a) by the green arrows. Rietveld analyses have shown that the $Acaa$ structural phase exhibits a UNTE [7], identical to that of the $I4_1/acd$ space group of the homologous Ca_2MnO_4 structure [8,14]. Ablitt *et al.* attributed the layering of the RP structures and the condensations of X_1^- MnO_6 to the octahedra distortion fundamental in the enhancement of the elastic anisotropy that drives the UNTE, in the presence of a thermal force imposed mainly by $Ca_3Mn_2O_7$ soft phonon modes [8].

Liu *et al.* also characterized the $Ca_3Mn_2O_7$ crystal structure, as a function of temperature, by XRD using Cu $K\alpha$ radiation [11]. It was stated that the results fit well the low-symmetry $A2_1am$ at low temperatures (207 K), and the high-symmetry $I4/mmm$ at high temperature (673 K). Within this temperature window, ~600–300 K, a mixture of multiple structures, including the $I4/mmm$, $A2_1am$, and $Amam$ phases, was also reported. These observations are not in agreement though with the structural phase diagram recently published in Ref. [14], that compiles the previously published information in Ref. [7] with further extended structural measurements up to 1150 K. In the structural phase diagram, the polar $A2_1am$ structure, that is observed at room temperature, coexists solely with the $Acaa$ phase, which seems to persist even up to 1150 K [14]. Unlike the results of Liu *et al.*, no evidence for the presence of the $I4/mmm$ phase within this temperature range was given [7,14]. Table I summarizes the experimental parameters reported in Refs. [7,14], at room temperature, for

TABLE I. Published information on the crystallographic phases of $Ca_3Mn_2O_7$: structural parameters refined at 300 K, respective observable temperature range, and functional properties [7,14].

Space group	a (Å)	b (Å)	c (Å)	Temp. range (K)	Functional properties
$A2_1am$	5.2376	5.2459	19.4501	0–350	Ferroelectric; AFM-G
$Acaa$	5.2152	5.2152	19.6156	200–1150	Uniaxial NTE

the $A2_1am$ and $Acaa$ phases, the respective temperature range of observation, and the known physical functionalities.

The present work provides a nanoscopic scale view of the $Ca_3Mn_2O_7$ atomic environment, relying on a detailed measurement of the electric field gradient (EFG). The use of perturbed angular correlation (PAC) experiments combined with simulations in the DFT framework provide a unique tool to characterize the $Ca_3Mn_2O_7$ structural transitions at the atomic scale. The nanoscopic characterization of the Ca site local environment allows one to accurately probe, particularly, the MnO_6 octahedral rotations that underlie the material's structural transitions and their correlation with novel functional properties. The sensitivity of the PAC observable is temperature independent, allowing one to explore a wide range of temperatures, and its sensitivity to small distortions around the probe nucleus allows one to study the structural phase transitions at their initial nucleation stages. Moreover, combining such local atomic-scale experimental information with *ab initio* DFT simulations, we are able to ultimately clarify the structural path that the $Ca_3Mn_2O_7$ follows from the high-temperature $I4/mmm$ symmetry, through the $Acaa$ one, before achieving the low-temperature ferroelectric $A2_1am$ symmetry. We also observe that, locally, the ferroelectric $A2_1am$ low-temperature phase persists much above room temperature, up to $\approx$500 K.

II. METHODS

A. Experimental details

Polycrystalline samples of $Ca_3Mn_2O_7$ were prepared by solid state reaction of mixed stoichiometric quantities of $CaCO_3$ (99.0%; Sigma-Aldrich) and MnO_2 (99.99%; Sigma-Aldrich). The mixture was calcinated for 3 h at 1123 K in air. Three more grinding and subsequent 12-h 1648 K annealing steps were performed. Single phase purity was confirmed by Le Bail refinement on the x-ray powder diffraction data collected with a Rigaku smartlLab diffractometer and analyzed with the FULLPROF software package [15]. The extracted structural parameters are presented in Appendix A.

To perform the PAC experiments [16], individual $\sim$0.5-mm^3 samples from the same batch material were first implanted at ISOLDE-CERN with radioactive ^{111m}Cd ($t_{\frac{1}{2}}$ = 49 min), at 30 keV energy, to a low dose of 10^{11} Cd/cm^2, below 1 ppm of the Ca/Mn atomic concentrations. Before the PAC measurement started, a 20 min annealing at 1123 K in air was performed on every sample, to recover from implantation damage. The recovery of point defects and the incorporation of the Cd probe at the right lattice sites were certified by the PAC measurement itself, leading to well-defined $R(t)$ experimental anisotropy functions, the characteristic PAC observable. Each temperature measurement took $\sim$3 h acquisition time using a 6-BaF_2 detector spectrometer [17] equipped with a dedicated closed-cycle refrigerator or with a special high-temperature furnace. Low-temperature measurements were done with the sample in vacuum; above room temperature the measurements were done with the sample in air. Due to the short lifetime of the parent ^{111m}Cd probe, to cover a wide temperature range of measurements, from 10 K up to 1200 K, every temperature point required a new implantation-annealing measurement of $\sim$4 h cycling. For further experimental details see, e.g., Refs. [18,19]. Due to the similar ionic radii and the same cation valences, Cd^{2+} probe ions easily substitute Ca^{2+} (Ref. [20]).

The $R(t)$ experimental function was fitted with exact numerical methods that build the expected observable by solving the characteristic equations of the hyperfine interaction Hamiltonian [16,19,21–23].

The EFG, characterizing the external charge density that interacts with the probe nucleus, is described by a second-order traceless symmetric tensor. In the principal reference frame, where the EFG is diagonal, the principal component V_{zz}, defined such as $|V_{zz}| \geqslant |V_{yy}| \geqslant |V_{xx}|$, and the asymmetry parameter $\eta = (V_{xx} - V_{yy})/V_{zz}$, fully characterize the observable hyperfine interaction [16]. In case of static electric quadrupole interactions, a time-dependent perturbation factor on the observable gamma-ray angular anisotropy of the decay cascade can be described as a sum of periodic terms which are further shaped by an exponential term:

$$G_{kk}(t) = S_{k0} + \sum_n S_{kn} \cos(\omega_n t) e^{-\delta\omega_n t}. \quad (1)$$

The frequencies represented by ω_n are those of the transition frequencies between the hyperfine levels created when a nuclear state is split by the hyperfine interaction. In the case of ^{111}Cd, the intermediate level is characterized by nuclear spin momentum of $I = 5/2$. The quadrupole interaction splits this level into three sublevels and thus in the Fourier transforms (FTs) we observe a triplet of frequencies ($\omega_1, \omega_2, \omega_3 = \omega_1 + \omega_2$) for each nonvanishing EFG distribution present in the system. The transition frequencies ω_n, with relative width δ, and the correspondent amplitudes S_{kn} can be related with the fundamental quadrupolar frequency ω_0 [24]. In the particular case of $\eta = 0$, the fundamental quadrupolar frequency matches the lower observable, i.e., $\omega_1 = \omega_0$, being $\omega_2 = 2\omega_0$ and $\omega_3 = 3\omega_0$. The fundamental quadrupolar frequency can also be defined as

$$\omega_0 = \frac{\omega_Q}{6} = \frac{6e\hbar Q V_{zz}}{4I(2I-1)}, \quad (2)$$

where Q is the nucleus electric quadrupole moment.

For a static interaction, the anisotropy function obtained experimentally can be written as $R(t) = \sum A_{kk} G_{kk}(t)$ where A_{kk} are the angular correlation coefficients of the nuclear decay cascade and G_{kk} contains the perturbation of the angular correlation.

B. Computational details

The first-principles calculations were performed using the QUANTUM ESPRESSO computational package [25,26]. The electronic interactions were described within the DFT in the Kohn-Sham scheme [27,28], considering the exchange-correlation potential based on the generalized gradient approximation (GGA) as proposed by Perdew, Burke, and Ernzerhof [29]. The electronic wave functions were expanded using the projected augmented wave (PAW) method [30], with plane-wave cutoffs of 115 and 500 Ry for the wave function and density, respectively. The Brillouin zones for computing the electronic states were sampled by a Γ-centered $7 \times 4 \times 4$

Monkhorst-Pack **k**-point grid [31]. The PAW method has been proven to properly calculate hyperfine interactions [32].

As described, the $Ca_3Mn_2O_7$ bulk belongs to the class of RP materials, and can be characterized as a $(CaO)(CaMnO_3)_n$ compound, with $n = 2$, where the CaO rocksalt layers [Ca^{II}] alternate with double $CaMnO_3$ perovskite layers [Ca^{I}]. At low temperatures, the $Ca_3Mn_2O_7$ bulk crystallizes in the base-centered orthorhombic structure of the $A2_1am$ space group (No. 36). The conventional cell contains 48 atoms and the rhombohedral primitive cell has 24 atoms.

In order to obtain the ground-state properties, total energy minimization with respect to the changes in the atomic positions and cell parameters was performed to the point where the total force did not exceed 0.05 eV/Å, constraining the system to null internal pressure.

The *Acaa* (No. 68) phase of the $Ca_3Mn_2O_7$ is also a 48-atom base-centered orthorhombic conventional cell and a 24-atom rhombohedral primitive cell.

The computer simulations were performed using the primitive cells since, from the theoretical viewpoint, it is more interesting to use the cell that has as few atoms as possible, which is more efficient and less computational resource consuming, the respective structural representations of the primitive and conventional lattices of the $A2_1am$ and *Acca* phases are displayed in Appendix B.

In order to obtain the EFG tensor at the Ca sites of the $Ca_3Mn_2O_7$ compound as a function of temperature, the simulations were performed using the atomic positions obtained from experimental data [7], without atomic position optimization. Therefore, the electronic structure were calculated in the presence of sizable forces. Thus, each temperature indicated in the theoretical results corresponds, in fact, to the specific experimental atomic positions for such temperature.

The EFG main component V_{zz} and the asymmetry parameter η calculations were performed using the GIPAW package [33]. In order to validate the results obtained with the PAW formalism, some of the systems were also simulated with the full-potential linearized augmented plane wave method [34] using the WIEN2K code suite [35], which is a suitable all-electron method to obtain hyperfine parameters. These tests allowed one to verify that the values obtained with both methods were in good agreement, within a maximum relative difference of 10%, reasonably small considering the sensible nature of the hyperfine interactions.

In order to consider the inclusion of the Cd ion as a probe on the $Ca_3Mn_2O_7$ bulk, a 192-atom supercell ($2 \times 2 \times 2$) was constructed and a single Ca atom was replaced by a Cd one (Cd→Ca) in an appropriate position ([Ca^{I}] or [Ca^{II}]). The distance between a Cd probe and its periodic image was about 1 nm, which suffices to avoid any spurious Cd-Cd interactions.

Additional information about the $Ca_3Mn_2O_7$ DFT electronic and structural properties calculations is presented in Appendix B.

III. RESULTS

A. $Ca_3Mn_2O_7$ PAC results

Figure 2 (left) depicts representative experimental $R(t)$ anisotropy functions using ^{111m}Cd probes. The global fits to the $R(t)$ functions are shown by the thick continuous black lines in the spectra, and the respective FTs of the fits are also shown in Fig. 2 (right). The fits to the $R(t)$ experimental data were performed considering only electric quadrupole interactions. The static EFG distributions were assumed to be Lorentzian-like.

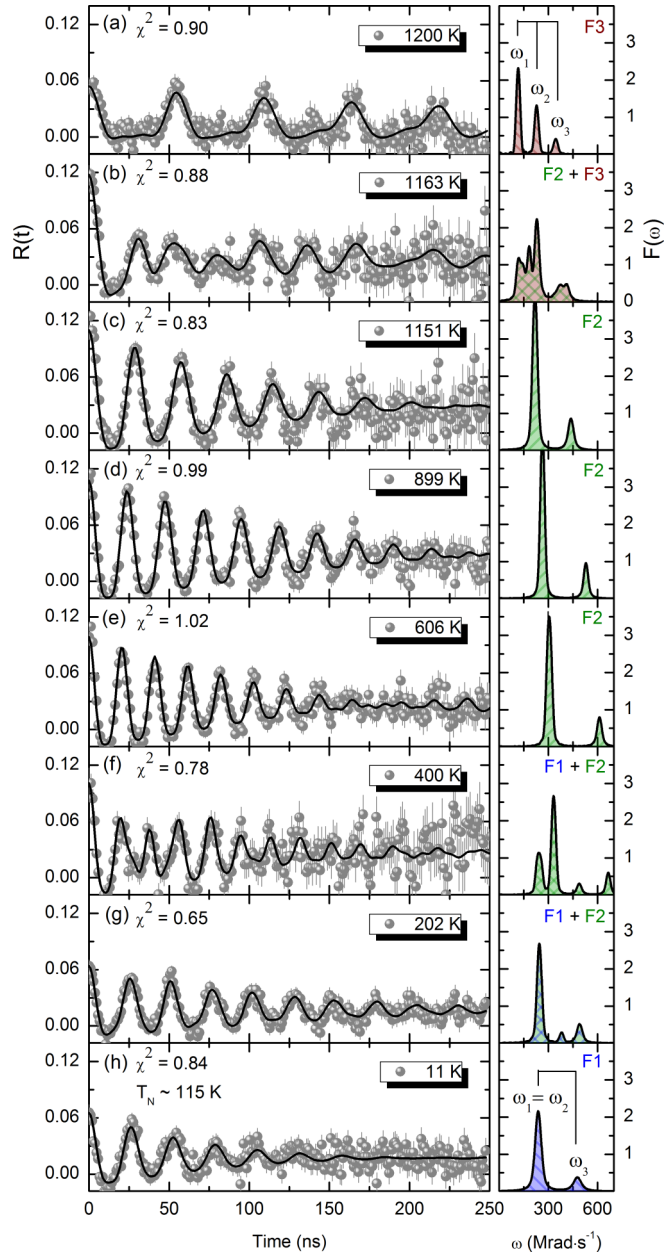

FIG. 2. Representative $R(t)$ functions, corresponding fits, and respective fit Fourier transforms taken at different temperatures for the ^{111}Cd parent probes in $Ca_3Mn_2O_7$.

By a simple inspection of Fig. 2 we can observe that the PAC results show clearly distinct regions in the temperature range from 1200 K to 10 K. In the highest temperature region, ranging from 1200 K to 1183 K, a single highly symmetric local environment, represented by an equidistant frequency triplet in the FT, can be observed and a representative spectrum is shown in Fig. 2(a); from 1151 K to 550 K, Figs. 2(c)–2(e), again, only one local environment is detected. Here, in the corresponding FTs, notice that, the first two

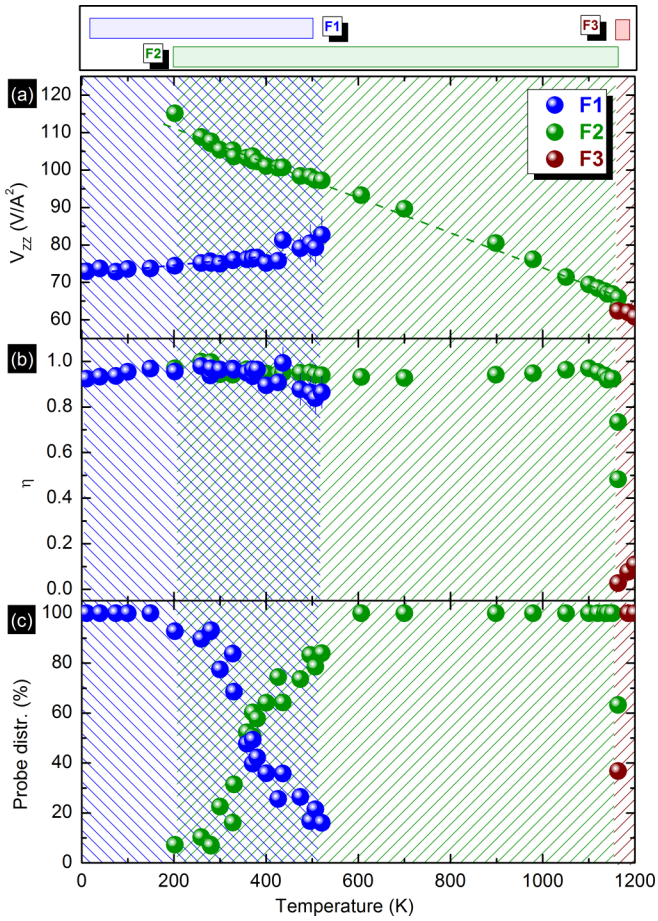

FIG. 3. Experimental EFG tensor at ^{111}Cd probe for the $Ca_3Mn_2O_7$ sample. (a) Principal component $|V_{zz}|$; (b) asymmetry parameter η; (c) probe distribution. The dashed lines are a guide for the eyes.

frequencies coincide, and a frequency doublet is observed, corresponding to a highly asymmetric EFG. Below 200 K, again, only one local environment is observed and Fig. 2(h) displays a representative spectrum of this temperature range. Figures 2(b), 2(f), and 2(g) show representative spectra of the other temperature regions where the coexistence of two local environments (two EFGs) is detected.

Moreover, our magnetization measurements have shown a paramagnetic to antiferromagnetic phase transition at $T_N =$ 115 K. Thus, below this magnetic phase transition, the magnetic hyperfine interaction between the canted antiferromagnetic ions and the probe nuclear magnetic dipole moment offers no abrupt change to the $R(t)$ function. Instead, a gradual increase of the $R(t)$ damping is observed for decreasing temperature, illustrated by comparing the $R(t)$ anisotropy function at 202 and 11 K, Figs. 2(g) and 2(h), and the respective FTs in which a larger line broadening is observed at 11 K.

Figure 3 summarizes the extracted parameters, obtained from the $R(t)$ fits, in the whole temperature range, where the thermal dependence of the EFG's parameters $|V_{zz}|$ and η are presented in Figs. 3(a) and 3(b), and in Fig. 3(c) local environment abundance is shown. At the lowest temperature, the EFG that emerges, here denoted as F1 environment, and identified as the blue dots in Fig. 3, presents a nonaxial symmetric EFG with $\eta \approx 1$ and $|V_{zz}| \approx 73$ V/Å^2. At intermediate temperatures, above 202 K and up to 1163 K, the EFG, here denoted as F2 environment and identified as green dots in Fig. 3, is also characterized by a highly nonaxially symmetric $\eta \approx 1$. This F2 EFG is easily distinguishable from the F1 environment by its higher $|V_{zz}| \approx 110$ V/Å^2, that decreases almost linearly with increasing temperature. The EFG measured at the highest temperatures, labeled as F3 environment and identified as the red dots in Figure 3, presents a $|V_{zz}|$ similar to the F2 one, but with a near axially symmetric local environment, $\eta \approx 0.11$, which is identified in the FT of Fig. 2(a) by the red shaded equidistant frequency triplet: ω_1, ω_2, and ω_3 with $\omega_2 \sim 2\omega_1$ and $\omega_3 \sim 3\omega_1$. Thus, overall, within the studied experimental temperature range, three local environments were unambiguously observed: F1, F2, and F3.

B. $Ca_3Mn_2O_7$ structural phase diagram at the local scale

For the $Ca_3Mn_2O_7$ system, structural data is available from literature, ranging from low temperature up to 1150 K [14]. In this temperature interval, after some controversy, two main phases were recently established by Senn *et al.* [7,14]. At the low-temperature region, the structural data was refined within a polar $A2_1am$ spatial group while a paraelectric *Acaa* phase was observed around room temperature and confirmed to be stable up to 1150 K. Above 1150 K there is no structural data. Nevertheless, by symmetry analysis the $I4/mmm$ space group is predicted [1,2], although not yet confirmed.

Taking into account this information, we thus associate the F1 phase, the blue shadowed region in Fig. 3, as the local fingerprint of the polar $A2_1am$ structural phase. Similarly, we associate the F2 phase, the green shadowed region in Fig. 3, as measured by PAC, with the *Acaa* space group. Comparing the herein results concerning the ferroelectric $A2_1am$ phase and the nonpolar *Acaa* one with the ones presented by Senn *et al.* [7] using high-resolution XRD, a wider range of coexistence, from 200 K to 500 K, is perceived with our local probe technique. In fact, the ferroelectric $A2_1am$ structure persists, when heating, up to 500 K, whereas it was previously shown that it should be almost fully converted to the *Acaa* phase around 350 K. Our results suggest the presence of small sized structural ferroelectric $A2_1am$ clusters within the *Acaa* matrix up to 500 K, still being around 50% of phase abundance at 350 K. The PAC technique has already given proof that it is able to detect the presence of small sized structural clusters, not easily detected with long-range structural characterization techniques [18,36].

The F3 phase, the red shadowed region in Fig. 3, characterized by a low-asymmetry parameter, is compatible with the $I4/mmm$ high-symmetry phase and is observed here only for temperatures higher than 1163 K, in contrast with the report presented by Liu *et al.* [11], which by standard XRD measurements claimed that the $I4/mmm$ phase should already be established at 673 K. The phase diagram recently published by Ablitt *et al.* shows that, within the range from $\approx$350 K to 1150 K, only the *Acaa* phase is observed [14], in agreement with our experimental observations. In the analog RP Sr_2RhO_4, synchrotron XRD studies show an apparent continuous structural transition, from the $I4_1/acd$ phase to

the $I4/mmm$ phase at ≈850 K, where the Mn-O-Mn distortion angle proceed in a continuous fashion towards 180°(Ref.[37]). However, we can observe that before the $I4/mmm$ structure is fully achieved ($\eta = 0$), the experimental $R(t)$ function measured at 1163 K can only be fitted properly considering three local environments with distinct η parameters. This indicates that the nature of the *Acaa* to the $I4/mmm$ structural transition may in fact be of the second-order type, where the coexistence of the local environments with distinct η parameters can be linked with different degrees of the MnO_6 octahedral rotation, still within the *Acaa* symmetry.

Complementary PAC measurements were also performed for a sequence of three measuring temperatures, 1163 K → 1185 K → 1100 K, showing that the structural phase transition *Acaa* to $I4/mmm$ is indeed a reversible transition. DFT calculations, shown in next section, confirm that the transition from the *Acaa* to the $I4/mmm$ structural phase should be perceived at the Cd probing site by a change from a low axial to a high axial symmetry.

C. DFT discussion on the evolution of the EFG parameters in the $A2_1am$, *Acaa*, $I4/mmm$ structures

Comparing the EFG parameters obtained experimentally with those obtained theoretically at the substitutional Cd, for both nonequivalent positions Cd^{I} or Cd^{II}, in the $Ca_3Mn_2O_7$ supercell in the $A2_1am$ phase presented in Appendix C, it is established that the Cd probes occupy preferably the Ca^{II} rocksalt position, explaining why the PAC experimental data can be fitted by using a single probing site per each structural phase. Energetic analysis estimated an energy difference of ≈300 meV/cell in favor of the nine-coordinated Ca^{II} sites. The supercell calculations also show that the introduction of the Cd probe hardly modifies the local environment of the Ca ions, especially when implanted at the Ca^{II} (rocksalt) sites. Thus the Cd-doped $Ca_3Mn_2O_7$ system can be modeled, in a first approximation, by using the structural parameters of the $Ca_3Mn_2O_7$ primitive cell. In this section we present a discussion on the nature of the opposite V_{zz} thermal tendencies exhibited by the $A2_1am$ and *Acaa* phases and the evolution of the asymmetry parameters that are expected for the $A2_1am$, *Acaa*, and $I4/mmm$ symmetries.

According to the initial theoretical descriptions, where the EFG is assumed to be proportional to the lattice contribution, the Bayer's Model later generalized by Kushida [38–40], the changes in V_{zz} with temperature result essentially from thermal expansion of the lattice parameters and thermal motion. For an ionic crystal and for an isotropic positive volume thermal expansion, a decrease of V_{zz} is expected when increasing temperature. Other important contributions must be sometimes considered, such as lattice vibrations that cause time-dependent EFG fluctuations (usually at frequencies of $\sim 10^{12}$ s^{-1}, much higher than the quadrupole frequency of $\sim 10^{8}$ s^{-1}, that actually result in the measurement of an average EFG) [39–41]. Kushida showed that if one considers harmonic vibrations around the atom's equilibrium positions, such as rotation modes, at sufficiently high temperatures ($k_BT \gg \hbar\omega$) the $|V_{zz}|$ should decrease linearly with increasing temperature [39,40], as identically observed in the

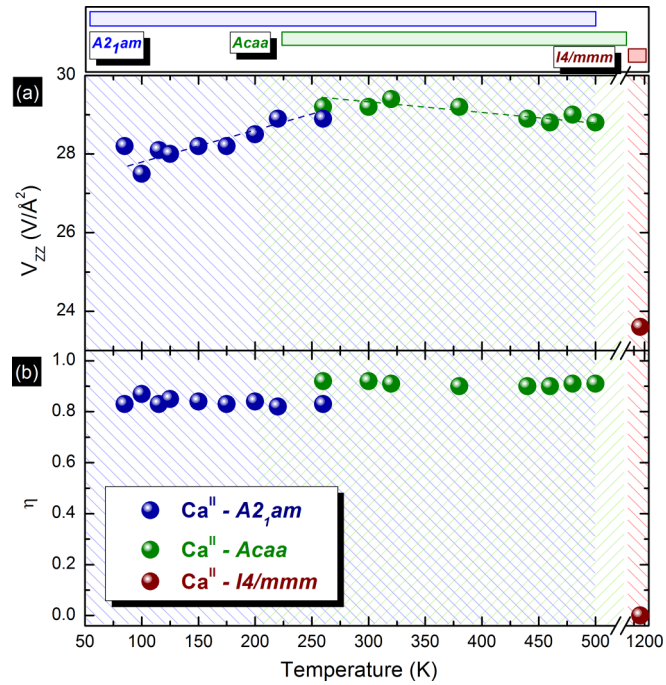

FIG. 4. Electric field gradient obtained with DFT in the rocksalt (Ca^{II}) sites of the $Ca_3Mn_2O_7$. (a) Principal component $|V_{zz}|$; (b) asymmetry parameter η. The blue shadowed region symbolizes the $A2_1am$ phase, the green one symbolizes the *Acaa* phase, and the red one the $I4/mmm$ phase. The dashed lines in panel (a) are a guide for the eyes. Each temperature corresponds to the specific experimental atomic positions for such temperature, except for the $I4/mmm$, where the structural parameters of a simulated relaxed structure were used.

Acaa structural phase within the 400–1163 K range, shown in Fig. 3(a). The *Acaa* phase follows this standard trend; however, the $A2_1am$ phase does not. DFT calculations allow one to correlate the evolution of the experimental EFGs with the change in charge distribution that occurs around the probe site, therefore DFT calculations for the EFGs at the probing Ca^{II} site were performed by using high-quality structural data available within the range of 85–500 K, as previously published in Ref. [7], without any structural optimization. This allowed one to discriminate the lattice thermal expansion and the evolution of the $Ca_3Mn_2O_7$ lattice distortions contribution to the $|V_{zz}|$ thermal tendencies of the $A2_1am$ and *Acaa* symmetries, excluding the above-mentioned phonon contribution.

Depicted in Fig. 4 are the DFT results of $|V_{zz}|$ and η, for $A2_1am$ and *Acaa* phases, as a function of temperature for the rocksalt (Ca^{II}) site. Figure 4(a) shows that when the calculation is performed for the $A2_1am$ phase, the $|V_{zz}|$ value increases when heating, while it decreases for the *Acaa* phase. Moreover, the *Acaa* phase presents the highest $|V_{zz}|$ values. This agrees with the experimental trend, shown in Fig. 3(a), where we observe that the $|V_{zz}|$ value increases for the $A2_1am$ phase and decreases for the *Acaa* phase when heating, and also, with the fact that the $|V_{zz}|$ values are higher for the *Acaa* phase between 0 and 500 K. Thus we see that the anomalous $|V_{zz}|$ thermal dependence in the $A2_1am$ phase can

be explained purely from the evolution of the $Ca_3Mn_2O_7$ structural parameters as the temperature is increased. A direct comparison between the DFT and experimental $|V_{zz}|(T)$ slopes cannot be made as DFT calculations ignore the phonon contributions.

Figure 4(b) shows DFT results for the evolution of the η parameter at the Ca^{II} site. In the $A2_1am$ phase, η values vary between 0.82 and 0.87 and in the *Acaa* phase, this quantity is almost constant, approximately 0.9. The η parameter is almost temperature independent and similar for both of these crystallographic phases, in full agreement with the PAC experimental behavior depicted in Fig. 3, where an η value of ≈ 1 was measured for both $A2_1am$ and *Acaa* phases. For comparison purposes we present in Appendix D the theoretical EFG parameters calculated at the nonprobed Ca^{I} site.

Despite the absolute values of the EFG parameters obtained from DFT at the Ca^{II} site being different from those obtained with PAC, the behavior of these quantities as a function of temperature are similar, in both $A2_1am$ and *Acaa* phases. An improved quantitative agreement is obtained in the supercell calculations of the $A2_1am$ probed structure, where the contribution of the Cd probe internal electron orbitals, which amplify both values of $|V_{zz}|$ and η, is accounted, as well as small structural relaxations around the probe location (see Appendix C).

DFT calculations were also performed for the $Ca_3Mn_2O_7$ high-temperature $I4/mmm$ structural phase using the relaxed atomic positions available from Materials Project source at the Catalyst Hub Structure Database [42], since there are no refined experimental structural data available around 1200 K. These results are also represented in Fig. 4 by the red symbols. A high $|V_{zz}| = 23.6$ V/Å^2 was obtained, i.e., a similar value to that found in the *Acaa* phase calculations, thus in fair agreement with our experimental results. Furthermore, in the absence of MnO_6 octahedral rotations the asymmetry parameter $\eta \approx 0$, agreeing with the experimental results measured at high temperatures, displayed in Fig. 3, show a transition from a local low axial (*Acaa*) to high axial symmetry ($I4/mmm$). By inspection of the EFG principal axis directions at the Ca^{II} in the $I4/mmm$ structure, one observes that the principal axis associated with the V_{zz} component at the Ca^{II} site is defined parallel to the $I4/mmm$ unit cell c axis. A high axial symmetry is expected at this site as the symmetry group of this Wyckoff position contains an axis of fourfold rotational symmetry, as can be intuitively guessed in the c-axis perspective representation of the $I4/mmm$ unit cell illustrated in Fig. 1. The breaking of this high axial symmetry is achieved in the first coordination shell of the Ca^{II} ion (a tricapped trigonal prism composed of nine oxygen ions) by the condensation of the octahedral distortion X_1^- or X_2^+ mode, respectively, in the *Acaa* or the $A2_1am$ phase, leading to the high experimental values for the asymmetry parameter of $\eta \approx 1$. Moreover, in the $A2_1am$ symmetry the extra X_3^- tilting mode and the Ca antiferroelectric displacement Γ_5^- mode results in a small local rotation of the EFG principal axes. With these local symmetry results, we thus confirm that the expected $I4/mmm$ phase stabilizes at high temperature in the $Ca_3Mn_2O_7$ system. We further establish that the *Acaa* $\rightarrow$ $I4/mmm$ phase transition occurs at around 1163 K.

IV. CONCLUSIONS

The measurement of the EFG combined with *ab initio* DFT calculations has shown to be a valuable tool to probe the MnO_6 octahedral rotations that lie behind the $Ca_3Mn_2O_7$ multiferroic and anisotropic thermal expansion properties. We measured the structural transition path that $Ca_3Mn_2O_7$ takes from the low-temperature $A2_1am$ polar phase to the high-temperature $I4/mmm$ predicted one, passing through the *Acaa* symmetry. Our combined experimental and *ab initio* study clearly confirms that the phase that stabilizes at the highest temperatures has the $I4/mmm$ symmetry, establishing also the critical temperature for this second-order phase transition to be around 1163 K.

Moreover, we have detected at the local scale, the presence of a hybrid improper ferroelectric $A2_1am$ phase up to 500 K, in contrast with previous macroscopic results that showed a near full conversion to the *Acaa* phase already at around 350 K.

Finally, we have shown the high preference for Cd to occupy the Ca rocksalt layer site in the $Ca_3Mn_2O_7$ structure. Following the design guidelines established for predicting novel hybrid improper ferroelectrics [3], we propose, based on the results presented here, the study of the $Cd_3Mn_2O_7$ and the $Cd_2CaMn_2O_7$ compounds, as novel hybrid improper ferroelectric and multiferroic materials.

ACKNOWLEDGMENTS

The authors acknowledge project NECL (Network of Extreme Conditions Laboratories) under NORTE-01-0145-FEDER-022096, POCI-01-0145-FEDER-029454, and POCI-01-0145-FEDER-032527, and FCT through EXPL/IF/00686/2014 and CERN/FIS-PAR/0005/2017. The authors also acknowledge funding from FAPESP Project 2018/07760-4, the German Federal Ministry of Education and Research (BMBF) through Contract No. 05K16PGA and the European Commission through the Horizon 2020 program Grants No. 734801 and No. 654002 (ENSAR 2, for supporting IS647 ISOLDE-CERN experiment). P.R.-R. gratefully thanks the FCT-Portugal for FCT Grant No. SFRH/BD/117448/2016. We also acknowledge support from CAPES and CNPq. L.V.C.A. (Project No. 305753/2017-7) and H.M.P. (Project No. 311373/2018-6) also acknowledge funding from CNPq.

APPENDIX A: CRYSTALLOGRAPHIC DATA OF STUDIED SAMPLE $Ca_3Mn_2O_7$

In Table II are presented the structural parameters for the $A2_1am$ and *Acaa* phases obtained by Profile matching fit

TABLE II. Crystallographic data of the $Ca_3Mn_2O_7$ sample.

T (K)	Space group	a (Å)	b (Å)	c (Å)	χ^2
300	$A2_1am$	5.23954	5.23840	19.42711	5.76
	Acaa	5.21189	5.21189	19.59600	

to data collected by Cu-K_α radiation x-ray diffraction for polycrystalline $Ca_3Mn_2O_7$ at room temperature.

APPENDIX B: ELECTRONIC AND STRUCTURAL PROPERTIES OF THE $Ca_3Mn_2O_7$ GROUND STATE

As experimentally and theoretically reported by previous works, at low temperatures, the $A2_1am$ phase of the $Ca_3Mn_2O_7$ system presents a G-type antiferromagnetism (AFM-G) as ground state [9]. This was also confirmed in our calculations, where the A-, C-, and G-type AFM configurations, as well as the ferromagnetic (FM) one were investigated—all with full relaxation. A major energy difference of $\approx$182 meV/cell in favor of the AFM-G state, with respect to the FM alignment, and a minor energy difference of $\approx$27 meV/cell with respect to the AFM-C state, also favoring the AFM-G configuration, were obtained. Therefore, herein, unless explicitly stated, it will always refer to this AFM-G structure when the ground state is mention.

Our calculations showed, after geometry optimization, that the ground state presented the primitive lattice parameters $a = 5.28$ Å and $b = c = 10.12$ Å and an angle $\alpha = 149.8°$ between the b and c axes, the respective structural representation of the primitive lattice of the $A2_1am$ and $Acca$ phases are displayed in Fig. 5 and Fig. 6. The Mn-O-Mn angles were 163.5° (equatorial oxygen atoms) and 158.4° (apical oxygen atoms), rather than 180° as in the ideal perovskite. These octahedral tilts are in agreement with the results of Lobanov *et al.* [9], which have observed the Mn-O-Mn bond angles in the range 160.6°–160.9° for the low-temperature $Ca_3Mn_2O_7$ compound. The spin magnetic moment values at the Mn sites, without considering any Hubbard correction on the Mn 3d states ($U = 0$), were $\pm 2.28 \mu_B$/atom.

Still considering null the Hubbard U parameter, the results showed that the AFM-G $Ca_3Mn_2O_7$ bulk in the $A2_1am$ structural phase, at $T = 0$ K, is an insulator, as expected, with a direct gap (Γ-Γ) of $\approx$0.8 eV. By introducing $U = 4.5$ eV (Ref. [1]), the gap increased to $\approx$1.0 eV and the Mn magnetic moments were enhanced to $\pm 2.66 \mu_B$/atom, due to the larger localization of the Mn-3d wave functions. The gap arises mainly from the energy difference (crystal field split) between

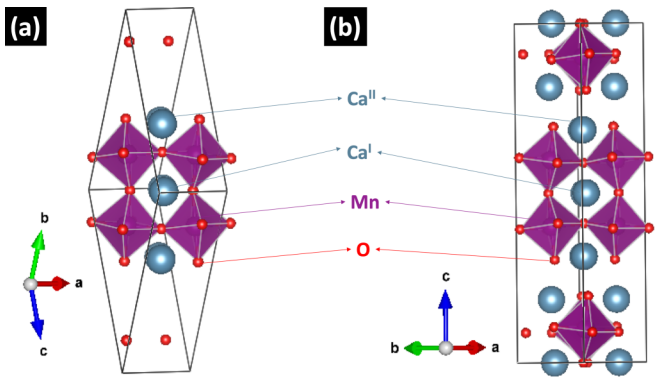

FIG. 5. Structural representation of the (a) primitive and (b) conventional lattices of the $Ca_3Mn_2O_7$ in the $A2_1am$ phase. The blue, red, and purple spheres represent the atoms of calcium, oxygen, and manganese, respectively.

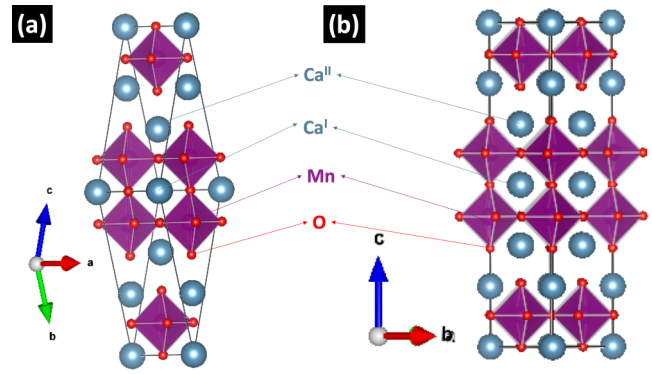

FIG. 6. Structural representation of the (a) primitive and (b) conventional lattices of the $Ca_3Mn_2O_7$ in the $Acaa$ phase. The blue, red, and purple spheres represent the atoms of calcium, oxygen, and manganese, respectively.

the Mn 3d-derived t_{2g} states fully occupied that constitute the top of the valence band, and the unoccupied e_g states on the bottom of the conduction band. Figure 7 shows the obtained electronic band structures of the $Ca_3Mn_2O_7$ bulk with and without considering the Mn-3d U correction. The gap value can be compared with the one obtained by Norton *et al.* [43], of 1.4 ± 0.1 eV. The values obtained for the Mn magnetic moment are in excellent agreement with the experimental value observed by Lobanov *et al.* [9], of $2.67 \pm 0.05 \mu_B$/atom, at $T = 10$ K, and the theoretical value calculated by Matar *et al.* [44], of $\sim 2.678 \mu_B$/atom.

APPENDIX C: ^{111m}Cd AS A PROBE WITHIN $Ca_3Mn_2O_7$ LATTICE

Although the assignment of the structural phases with our EFG local results is unambiguous, the local nature of the technique allows a precise atomic position assignment, within the unit cell, when our experimental data are compared with the theoretical DFT results. Table III shows the theoretical

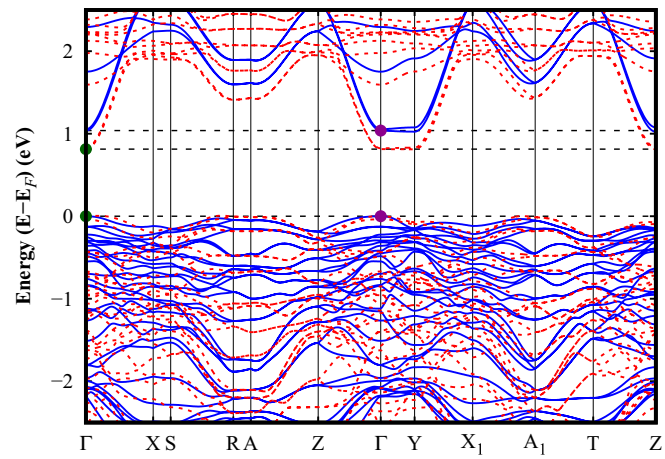

FIG. 7. Electronic band structure of the AFM-G $Ca_3Mn_2O_7$ compound in the $A2_1am$ structure, in the high-symmetry directions of the primitive cell Brillouin zone (see Fig. 5). Dotted (red) and solid (blue) lines present the GGA ($U = 0$) and GGA + U ($U = 4.5$ eV) results. The points represent the top of the valence band and the bottom of the conduction band. Plots are for one magnetic sublattice.

EFG results for the substitutional Cd at Ca^{I} or Ca^{II} atomic positions, in the AFM-G $Ca_3Mn_2O_7$ supercell in the $A2_1am$ phase. For comparison the respective values at the Ca sites in the undoped material are also shown. It is worth mentioning that the obtained values do not change considering either Hubbard U correction on the Mn $3d$ states or spin-orbit coupling.

In Table III, it can be observed that the Cd probe replacement at the Ca^{II} site increases the $|V_{zz}|$ values by a factor of ≈ 2, while for the replacement of the Ca^{I} site by Cd this factor is ≈ 2.5. In both cases, the η parameters are almost unchanged. Interestingly, this increase for Ca^{II} sites correlates with a simple Sternheimer picture, where the polarization of the probe's internal orbitals amplifies the EFG by the so-called Sternheimer antishielding effect. The contribution of the EFG arising purely from the ionic lattice [16] is increased by a factor that for Cd^{2+} and Ca^{2+} ions is ≈ 1.9 [45].

Comparing the EFG parameters obtained experimentally with those obtained theoretically for the $A2_1am$ $Ca_3Mn_2O_7$, shown in Table III, it is established that we are probing the rocksalt site ([Ca^{II}]). Also, tests were performed when one Ca atom was replaced by Cd in the $Ca_3Mn_2O_7$ primitive cell, without any relaxation, generating a 1:5 Cd concentration. The calculated hyperfine parameters at Cd^{II} are $|V_{zz}| = 53.9$ V/Å^2 and $\eta = 0.86$. These values are in very good agreement with the results obtained with the Cd-doped supercell, where the Cd concentration is 1:47 and the Cd nearest neighbors were allowed to relax. In turn, when we compare the obtained hyperfine parameters for Cd^{I}, which are $|V_{zz}| = 44.8$ V/Å^2 and $\eta = 0.55$ for the 1:5 Cd concentration in the primitive cell (without relaxation), we also observe good agreement with the doped supercell, but showing in this case that the effect of relaxation is more important than in the previous case. Interestingly, the electric hyperfine quantities are very robust and the system could be modeled by just using the primitive cell. These observations may serve to show that the introduction of the Cd probe hardly modifies the local environment of the Ca ions, especially in the Ca^{II} (rocksalt) sites.

Further, the DFT energetic analyses were performed to inspect the Cd most stable site: rocksalt or perovskite. The results of the Cd impurity in the 192-atom supercell, in each one of the two Ca sites, provided an energy difference of ≈ 300 meV/cell in favor of the nine-coordinated Ca^{II} sites.

TABLE III. EFG principal component $|V_{zz}|$ and asymmetry parameter η obtained for the AFM-G $A2_1am$ $Ca_3Mn_2O_7$ 192-atom supercell at the Cd site replacing the Ca atoms, at both nonequivalent positions Cd^{I} (perovskite) and Cd^{II} (rocksalt), together with the respective values at the Ca^{I} and Ca^{II} sites for the pristine $Ca_3Mn_2O_7$ compound. $|V_{zz}|$ is given in units of V/Å^2.

	$\lvert V_{zz}\rvert$	η
$Ca_3Mn_2O_7$:Cd^{I}	61.2	0.43
$Ca_3Mn_2O_7$:Ca^{I}	23.2	0.45
$Ca_3Mn_2O_7$:Cd^{II}	59.9	0.89
$Ca_3Mn_2O_7$:Ca^{II}	27.4	0.82

APPENDIX D: DFT COMPARISON OF THE EFG PARAMETERS IN THE $A2_1am$, $Acaa$, $I4/mmm$ STRUCTURES ON THE Ca^{I} AND Ca^{II} SITES

In Fig. 8 we present, for comparison, the evolution of the EFG parameters for the $A2_1am$, $Acaa$, and $I4/mmm$ phases for the nonequivalent Ca^{I} and Ca^{II} positions. Each temperature corresponds to the specific experimental atomic positions for such temperature, except for the results displayed for the $I4/mmm$ phase, where the relaxed atomic positions available from Materials Project source at the Catalyst Hub Structure Database [42] were used, since there are no refined experimental structural data available around 1200 K. Herein we discuss in more detail the DFT results obtained for the experimentally nonprobed Ca^{I} site.

By inspecting the EFG principal axis direction in the undistorted $I4/mmm$ phase of the $Ca_3Mn_2O_7$ compound, one observes that the V_{zz} principal axis at the Ca^{I} site is defined parallel to the $I4/mmm$ unit cell c axis. Unlike the Ca^{II} site that is surrounded by a tricapped trigonal prism composed of nine oxygen atoms, the coordination shell of the Ca^{I} site in the $I4/mmm$ phase corresponds to a cuboctahedron composed of 12 oxygen atoms, resulting in a lower V_{zz} magnitude ($|V_{zz}| = 4.5$ V/Å^2, $\eta = 0$) than the value obtained for the Ca^{II} site ($|V_{zz}| = 23.6$ V/Å^2, $\eta = 0$). On the other hand, in the Ca^{I} site the orientation of the V_{zz} principal axis is not defined by the first coordination shell, but by the symmetry

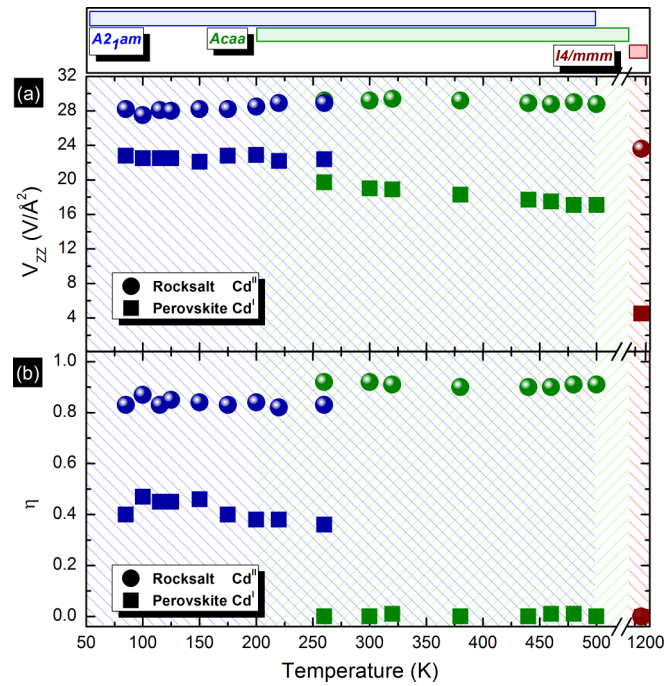

FIG. 8. Electric field gradient obtained with DFT in the Ca sites of the $Ca_3Mn_2O_7$, in the rocksalt (Ca^{II}; spheres) and perovskite (Ca^{I}; squares) sites. (a) Principal component $|V_{zz}|$; (b) asymmetry parameter η. The blue shadowed region symbolizes the $A2_1am$ phase, the green one symbolizes the $Acaa$ phase, and the red one the $I4/mmm$ phase. Each temperature corresponds to the specific experimental atomic positions for such temperature, except for the $I4/mmm$, where the structural parameters of a simulated relaxed structure were used.

breaking imposed by the layer stacking along the c axis of the Ruddlesden-Popper structure.

In contrast to the Ca^{II} site, the calculated η parameter at the Ca^{I} site exhibits a discontinuity $\Delta\eta \approx 0.35$ when shifting from the *Acaa* to the $A2_1am$ phase. For the *Acaa* phase, in the condensation of the X_1^- octahedral distortion mode, the adjacent neighboring MnO_6 octahedra rotate in an antiphase mode, such that the equatorial oxygen atoms of each pair of adjacent MnO_6 octahedra rotate in opposite directions. Therefore, the axial symmetry of the EFG tensor at the Ca^{I} site is maintained when going from the $I4/mmm$ to the *Acaa* crystalline structure ($\eta \approx 0$). Nevertheless, in the $A2_1am$ phase the X_2^+ in-phase rotation mode of the MnO_6 octahedra is sufficient to reduce the EFG axial symmetry at the Ca^{I} site. In addition, the local coordination is further distorted by the X_3^+ tilting mode and the Ca antiferroelectric displacement Γ_5^- mode. In fact, the V_{zz} principal axis suffers a rotation from the c axis into the ab plane when going from the *Acaa* to the $A2_1am$ phase.

[1] N. A. Benedek and C. J. Fennie, Phys. Rev. Lett. **106**, 107204 (2011).

[2] N. A. Benedek, A. T. Mulder, and C. J. Fennie, J. Solid State Chem. **195**, 11 (2012).

[3] A. T. Mulder, N. A. Benedek, J. M. Rondinelli, and C. J. Fennie, Adv. Funct. Mater. **23**, 4810 (2013).

[4] M. J. Pitcher, P. Mandal, M. S. Dyer, J. Alaria, P. Borisov, H. Niu, J. B. Claridge, and M. J. Rosseinsky, Science **347**, 420 (2015).

[5] Y. S. Oh, X. Luo, F. T. Huang, Y. Wang, and S. W. Cheong, Nat. Mater. **14**, 407 (2015).

[6] Y. Wang, F.-T. Huang, X. Luo, B. Gao, and S.-W. Cheong, Adv. Mater. **29**, 1601288 (2017).

[7] M. S. Senn, A. Bombardi, C. A. Murray, C. Vecchini, A. Scherillo, X. Luo, and S. W. Cheong, Phys. Rev. Lett. **114**, 035701 (2015).

[8] C. Ablitt, S. Craddock, M. S. Senn, A. A. Mostofi, and N. C. Bristowe, npj Comput. Mater. **3**, 44 (2017).

[9] M. V. Lobanov, M. Greenblatt, E. A. N. Caspi, J. D. Jorgensen, D. V. Sheptyakov, B. H. Toby, C. E. Botez, and P. W. Stephens, J. Phys.: Condens. Matter **16**, 5339 (2004).

[10] K. Momma and F. Izumi, J. Appl. Crystallogr. **44**, 1272 (2011).

[11] M. Liu, Y. Zhang, L.-F. Lin, L. Lin, S. Yang, X. Li, Y. Wang, S. Li, Z. Yan, X. Wang *et al.*, Appl. Phys. Lett. **113**, 022902 (2018).

[12] J. F. Scott, C. A. Araujo, H. B. Meadows, L. D. McMillan, and A. Shawabkeh, J. Appl. Phys. **66**, 1444 (1989).

[13] B. Gao, F.-T. Huang, Y. Wang, J.-W. Kim, L. Wang, S.-J. Lim, and S.-W. Cheong, Appl. Phys. Lett. **110**, 222906 (2017).

[14] C. Ablitt, A. A. Mostofi, N. C. Bristowe, M. S. Senn, and A. Sanson, Front. Chem. **6**, 455 (2018).

[15] J. Rodríguez-Carvajal, Phys. B (Amsterdam, Neth.) **192**, 55 (1993).

[16] G. Schatz and A. Weidinger, *Nuclear Condensed Matter Physics: Nuclear Methods and Applications* (Wiley, New York, 1996).

[17] T. Butz, S. Saibene, T. Fraenzke, and M. Weber, Nucl. Instrum. Methods Phys. Res., Sect. A **284**, 417 (1989).

[18] A. M. L. Lopes, J. P. Araújo, V. S. Amaral, J. G. Correia, Y. Tomioka, and Y. Tokura, Phys. Rev. Lett. **100**, 155702 (2008).

[19] A. M. Lopes, J. P. Araújo, J. J. Ramasco, V. S. Amaral, R. Suryanarayanan, and J. G. Correia, Phys. Rev. B **73**, 100408(R) (2006).

[20] A. Lopes, J. Araújo, E. Rita, J. Correia, V. Amaral, Y. Tomioka, Y. Tokura, and R. Suryanarayanan, J. Magn. Magn. Mater. **272-276**, E1667 (2004).

[21] J. G. Correia, NNFIT and FFT upgrades, 2018.

[22] N. P. Barradas, NNFIT the PAC Manual,1992.

[23] N. P. Barradas, M. Rots, A. A. Melo, and J. C. Soares, Phys. Rev. B **47**, 8763 (1993).

[24] T. Butz, Hyperfine Interact. **52**, 189 (1989).

[25] P. Giannozzi, O. Andreussi, T. Brumme, O. Bunau, M. B. Nardelli, M. Calandra, R. Car, C. Cavazzoni, D. Ceresoli, M. Cococcioni *et al.*, J. Phys.: Condens. Matter **29**, 465901 (2017).

[26] P. Giannozzi, S. Baroni, N. Bonini, M. Calandra, R. Car, C. Cavazzoni, D. Ceresoli, G. L. Chiarotti, M. Cococcioni, I. Dabo *et al.*, J. Phys.: Condens. Matter **21**, 395502 (2009).

[27] P. Hohenberg and W. Kohn, Phys. Rev. **136**, B864 (1964).

[28] W. Kohn and L. J. Sham, Phys. Rev. **140**, A1133 (1965).

[29] J. P. Perdew, K. Burke, and M. Ernzerhof, Phys. Rev. Lett. **78**, 1396 (1997).

[30] P. E. Blöchl, Phys. Rev. B **50**, 17953 (1994).

[31] H. J. Monkhorst and J. D. Pack, Phys. Rev. B **13**, 5188 (1976).

[32] H. M. Petrilli, P. E. Blöchl, P. Blaha, and K. Schwarz, Phys. Rev. B **57**, 14690 (1998).

[33] T. Charpentier, Solid State Nucl. Magn. Reson. **40**, 1 (2011).

[34] *Planewaves, Pseudopotentials, and the LAPW Method*, 2nd ed., edited by D. J. Singh and L. Nordström (Springer, New York, 2006).

[35] P. Blaha, K. Schwarz, G. K. H. Madsen, D. Kvasnicka, and J. Luitz, *WIEN2K, An Augmented Plane Wave + Local Orbitals Program for Calculating Crystal Properties* (Karlheinz Schwarz, Techn. Universität Wien, Austria, 2001).

[36] G. N. P. Oliveira, A. M. Pereira, A. M. L. Lopes, J. S. Amaral, A. M. dos Santos, Y. Ren, T. M. Mendonça, C. T. Sousa, V. S. Amaral, J. G. Correia, and J. P. Araújo, Phys. Rev. B **86**, 224418 (2012).

[37] B. Ranjbar and B. J. Kennedy, Solid State Sci. **49**, 43 (2015).

[38] H. Bayer, Z. Phys. **130**, 227 (1951).

[39] T. Kushida, J. Sci. Hiroshima Univ., Ser. A Phys. Chem. **19**, 327 (1955).

[40] T. Kushida, G. B. Benedek, and N. Bloembergen, Phys. Rev. **104**, 1364 (1956).

[41] T.-C. Wang, Phys. Rev. **99**, 566 (1955).

[42] A. Jain, S. P. Ong, G. Hautier, W. Chen, W. D. Richards, S. Dacek, S. Cholia, D. Gunter, D. Skinner, G. Ceder *et al.*, APL Mater. **1**, 011002 (2013).

[43] M. Norton, R. Tom, and W. Glaunsinger, J. Solid State Chem. **48**, 242 (1983).

[44] S. F. Matar, V. Eyert, A. Villesuzanne, and M.-H. Whangbo, Phys. Rev. B **76**, 054403 (2007).

[45] P. C. Schmidt, K. D. Sen, T. P. Das, and A. Weiss, Phys. Rev. B **22**, 4167 (1980).